



Effect of Mold Cavity Design on the Thermomechanical Behavior of Solidifying Shell During Microalloyed Steel Slab Continuous Casting

ZHENYU NIU, ZHAOZHEN CAI, and MIAOYONG ZHU

Corner transverse cracks are frequently observed on microalloyed steel slabs during continuous casting. As a solution to this problem, double phase-transformation technology could improve the ductility of the shell surface and avoid corner cracks. However, this technology requires a high cooling rate, which is difficult to reach in traditional flat plate molds (TFMs). Therefore, a novel convex structure mold (NCM) was designed to intensify corner cooling. To investigate the effects of mold design on interfacial heat transfer between the solidifying shell and mold, a thermomechanical model was developed considering the dynamic distributions of the mold slag layers and air gaps. Afterward, the interfacial heat fluxes between mold and solidifying shell obtained from the thermomechanical model were loaded on the flow, heat transfer, and solidification model to study the comprehensive influence of mold cavity design and steel flow on the shell temperature. Based on the models, the contact conditions, distributions of interfacial heat transfer media, interfacial heat fluxes, and temperatures and thicknesses of the solidifying shells were thoroughly compared between the TFM and NCM. The results show that the NCM provides a more appropriate compensation for the shell shrinkage; as a result, the thick slag layers concentrating in the corners of the TFM are flattened and homogenized in the NCM. Thicker slag layers in the TFM weaken the corner heat transfer and lead to uneven shell growth in the off-corner area. Meanwhile, the NCM could homogenize the off-corner heat transfer and increase the cooling rate of the shell corner to help implement double phase-transformation technology in the high-temperature zone of casters.

<https://doi.org/10.1007/s11663-021-02123-8>

© The Minerals, Metals & Materials Society and ASM International 2021

I. INTRODUCTION

THERMAL shrinkage is an inherent characteristic of shells solidified in molds during continuous casting, which tends to pull the shells back from the hot mold faces. Effected by multiple factors, such as thermal shrinkage, haul force, ferrostatic pressure, and metal creep, the initial solidifying shell undergoes a complicated distortion in the primary cooling stage.^[1–4] If the distortion leads to undesirable contact conditions between the shell and copper plates of the mold, the temperature and solidification of the shell would be

uneven, which may cause defects on the slab/billet. To keep the mold in close contact with the solidifying shell, most molds have a tapered cavity designed to compensate for shell shrinkage.^[5,6]

During slab continuous casting, considerable shell shrinkage occurs along the width direction. Whether the taper of the narrow face could properly compensate for the shrinkage has a significant influence on the surface and subsurface quality of the slab. Won *et al.*^[7] found that excessive taper inevitably increases the friction between the strand and mold copper plates, which would expedite the wear of narrow face copper plates. Mahapatra *et al.*^[8] indicated that excessive compensation is a critical cause of longitudinal depressions and associated subsurface cracks. Brimacombe *et al.*^[9] indicated that an inadequate taper would enhance the tensile strain at the wide face of the slab, which subsequently leads to longitudinal mid-face cracks. Therefore, appropriate taper compensation is quite important for high-quality and high-efficiency slab production.

ZHENYU NIU, ZHAOZHEN CAI, AND MIAOYONG ZHU are with the State Key Laboratory of Rolling and Automation, Northeastern University, Shenyang 110819, China and also with the School of Metallurgy, Northeastern University, Shenyang 110819, China. Contact-email: caizz@smm.neu.edu.cn

Manuscript submitted September 21, 2020; accepted February 8, 2021.

Article published online March 23, 2021.

Currently, there are two mainstream taper compensation methods: the single linear taper and discrete multitaper methods. The single linear taper method is the most widely used in slab continuous casting because of its concise design and convenient machining. However, Li and Thomas^[2] indicated that the thermal shrinkage of a solidifying shell is nonlinear: the upper part of the mold needs a large taper to compensate for the considerable shrinkage of the solidifying shell, whereas the lower part needs a smooth taper to decrease the friction between the copper plates and slow-shrinking shell. Therefore, the single linear taper method can hardly maintain the close contact between the shell surfaces and mold hot faces in all parts of the mold. Although the multitaper method can compensate for the nonlinear shrinkage of the solidifying shell more appropriately, and extend the mold life to a certain extent by retarding the wear of the narrow face copper plates,^[10] a study by Berdnikov *et al.*^[11] showed that the multitaper method can hardly result in a seamless contact because the shrinkages of the slab corner and mid-face are out of sync. To compensate for the considerable corner shrinkage, Cai and Zhu^[12] suggested additional compensation for the narrow face corner. Since the compensation for shell shrinkage along the thickness direction is not changed, this method can hardly control the interfacial gap at the wide face side of the corner. A superior quality steel product demands a more appropriate taper compensation method.

Aiming at improving the quality of continuous casting steel, Brimacombe and Sorimachi^[13] investigated the influences of continuous casting operating conditions on the formation of different types of cracks. They concluded that the large corner gap resulting from the inadequate taper is the primary factor leading to longitudinal corner cracks, and the temperature gradient of the shell corner in the spray zone accounts for the frequent occurrence of transverse corner cracks. To homogenize the heat transfer of shell corners, Hu *et al.*^[14] suggested the chamfered mold as a solution to control the formation of transverse corner cracks. Based on their numerical study, the chamfered mold could increase the slab corner temperature. As a result, the corner stress at the straightening point is reduced. To further optimize the corner structure of chamfered molds, Yu *et al.*^[15] developed a numerical model with which the frictions between strands and molds with different corner structures were studied. The friction stress becomes more uniform in the fillet mold than it does in the chamfered and right-angle molds. In the study by Lyu *et al.*,^[16] a mold simulator system was used to compare the oscillation marks, interfacial heat fluxes, growth of shell thicknesses, and other solidification behaviors of initial solidifying shells between right-angle and chamfered molds. They found that the temperature distribution of the slab corner became higher and more uniform in the chamfered mold. Furthermore, a study by Filatov *et al.*^[17] showed that the application of a chamfered mold could homogenize the shell thickness and reduce crack formation in the rolled slab.

Undoubtedly, chamfered molds have many advantages over traditional right-angle molds. However, the high temperature of the slab corner tends to induce ferrite films to form along the austenite boundaries, which are believed to be the most significant cause of corner transverse cracks during microalloyed steel slab continuous casting.^[18] To inhibit the formation of corner transverse cracks, Kato *et al.*^[19] suggested a novel cooling method named surface structure control cooling (SSC) in which cooling on the shell surface is intensified before the slab corner reaches the A3 transformation temperature and then the shell corner is reheated to 1250 K. This method had been verified experimentally, and it was found that SSC could improve steel ductility by eliminating film-like ferrite.^[20] Furthermore, Liu *et al.*^[21] studied the refinement of prior austenite grains under double phase-transformation technology by the high-temperature confocal laser scanning microscope (CLSM). They concluded that the higher cooling rate during the first phase transformation leads to a finer austenite microstructure, which has a strong inhibition effect on cracks. Through the CLSM inspection, Ma *et al.*^[22] confirmed that the optimum cooling rate to eliminate film-like ferrite is 3 to 6 °C/s, which is not feasible with chamfered and right-angle molds. To enhance the cooling rate of the slab corner, the cavity structure of the mold should be precisely designed to guarantee close contact between the shell surfaces and mold inner walls.

Previous studies have shown that the design of slab mold tapers is rather complex because of the nonlinear shrinkage of shells. Moreover, the nonsynchronized shrinkage between the mid-face and corner of the slab intensifies this complexity. Although the chamfered mold can homogenize the corner heat transfer, the high temperature of the slab corner would aggravate the ductility of microalloyed steel by expediting the eutectoid of film-like ferrite along austenite boundaries. To control the corner microstructure of microalloyed steel during slab continuous casting, double phase-transformation technology has been suggested in many previous works, which demands a higher cooling rate at the slab corners during the first phase transformation. Aiming at precise taper compensation and a high cooling rate at the shell corner, a novel convex structure mold is designed, which could compensate for the shell shrinkage in the width direction by the gradient convex structure and that in the thickness direction by the nonlinear structure. The detailed design process will be presented in future work. In the present work, the comparison between the novel convex structure mold and traditional flat plate mold was conducted primarily to confirm the potency of novel design in improving the corner heat transfer of thick slabs. Through developing numerical models, the contact conditions and dynamic distributions of interfacial heat transfer media in the novel convex structure mold and traditional flat plate mold are compared. Subsequently, the effects of lubricant distributions on the corner and off-corner heat transfer are thoroughly discussed. It is expected that the novel convex structure mold will improve the ductility of

slab corners by helping to realize double phase-transformation technology during microalloyed steel continuous casting.

II. MODEL DESCRIPTION

A. Mold Geometry

Considering that the traditional flat plate mold (TFM) with a single linear taper is the most widely used in slab continuous casting, it is selected as the referenced mold, in which the thermomechanical behaviors of the slab shell are compared with those in the novel convex structure mold (NCM). Figure 1 shows half of the wide face copper plate that could be commonly used in both the TFM and NCM. At the back of the copper plate, there is a periodic layout of the channels, among which the depths of those near the bolt columns are 15 mm, and the others are 11 mm. The left view shows that the height of the channels is 850 mm. Additionally, the Ni layer thickness linearly ranges from 0.5 mm at the mold top to 1.5 mm at the mold bottom. Detailed locations of the channels and bolts can be found in Figure 1.

Figure 2 shows the narrow face copper plate of the referenced TFM. The thickness of the copper plate is 40 mm, and there are 8 shallow channels and 4 deep channels at its back. The deep channels on the margin have an outward inclination of 15 deg, which is designed to enhance corner cooling. The Ni layer gradient and detailed channel structure are identical to those of the wide face.

Based on the deformation of the slab shell in a continuous casting mold,^[23] a mold with a convex structure of narrow face copper plates is designed to reduce the corner gap between the mold and strand, as shown in Figure 3. At the top, the hot face bulges outward by 20 mm. Along the casting direction, the bulge gradually flattens, which presses the narrow face of the solidifying shell during continuous casting and extends the shell corner toward the wide face copper plate. As a result, the interfacial gap at the wide face corner may be reduced by the extension of the solidifying shell along the narrow face. Considering that the increased contact pressure at the narrow face center would also drive the shell corner to move toward the mold center, additional compensation is attached to the margin of the NCM. The projection of bulges at the top and bottom of the NCM as well as the additional compensation at the margin are quantified in Table I.

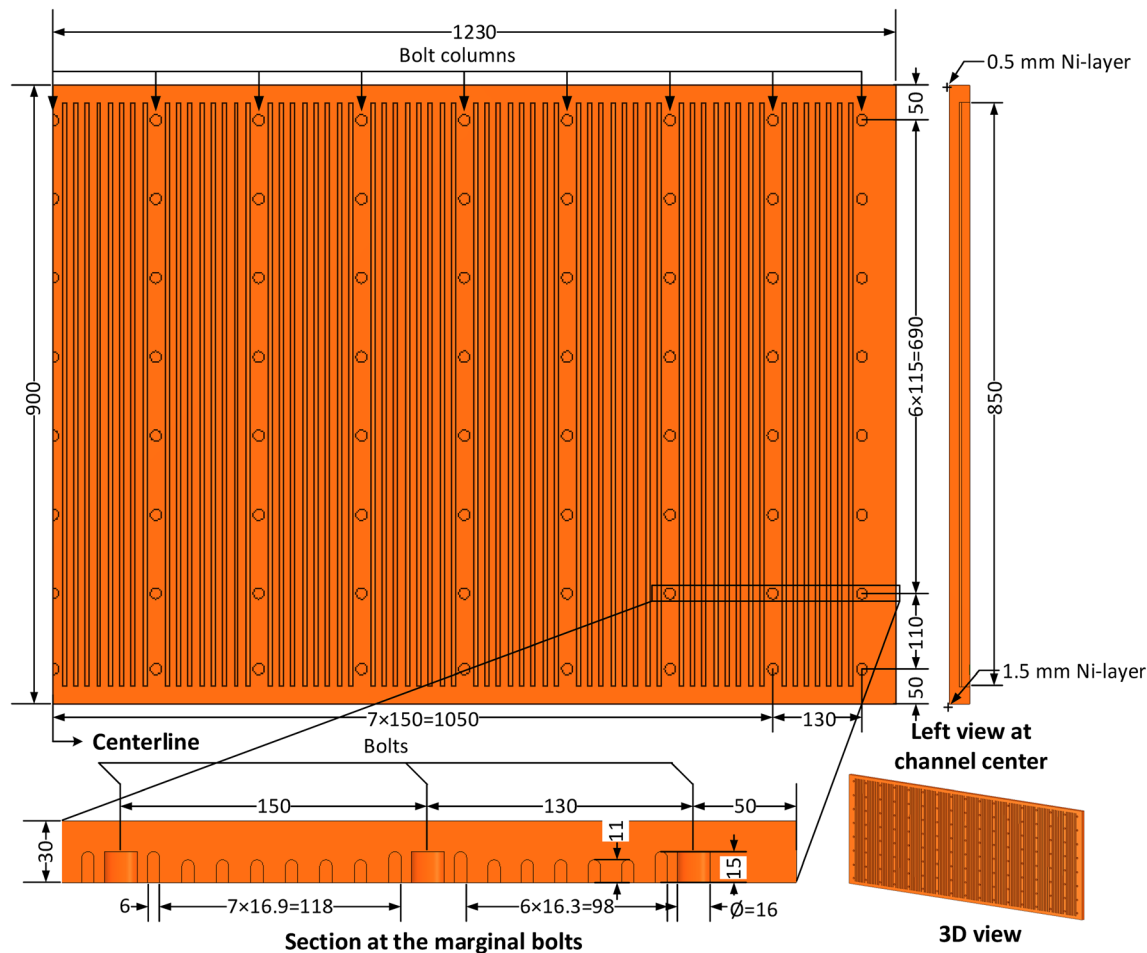


Fig. 1—Geometry of the wide face copper plate.

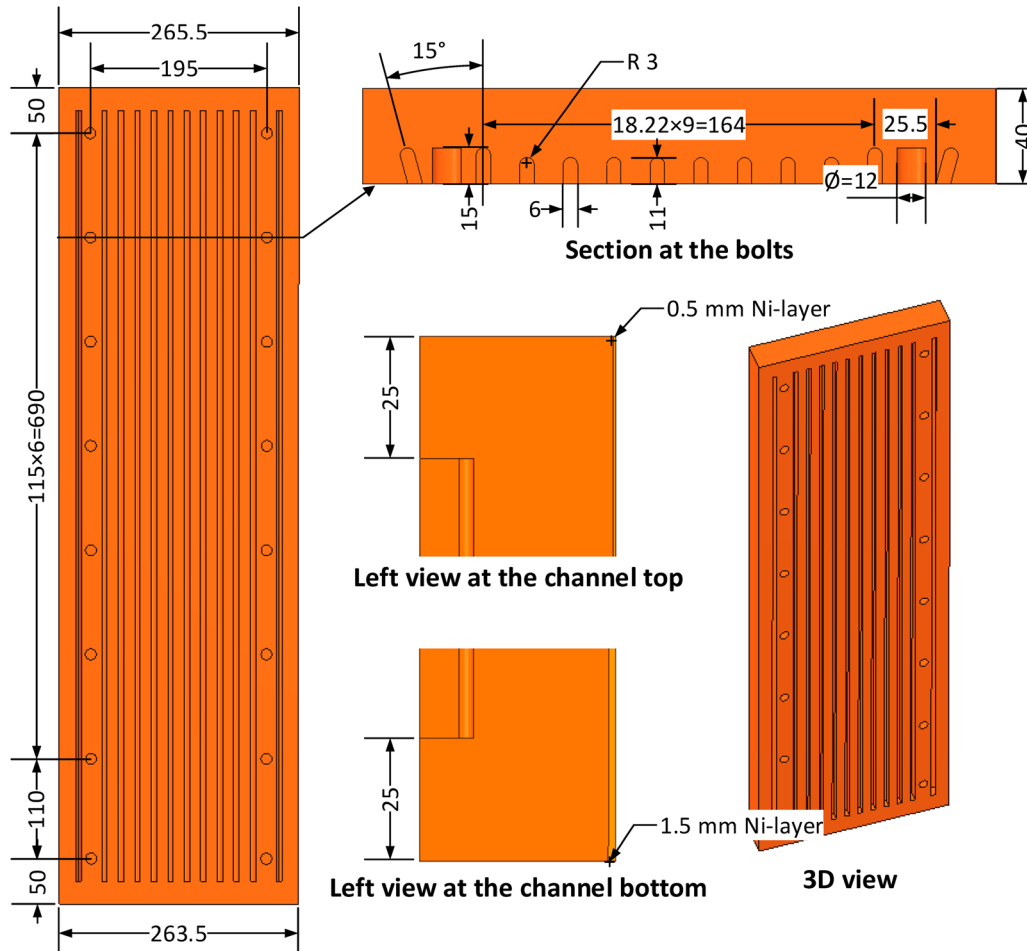


Fig. 2—Geometry of the narrow face copper plate of the TFM.

B. Mathematical Model

1. Thermomechanical model of continuous casting mold

A thermomechanical model based on the nonlinear finite element commercial software MSC Marc^[24] was developed to evaluate the effects of mold design on the thermal evolution and deformation behavior of solidifying shells, as shown in Figure 4. Considering the symmetry along the width and thickness directions, only one-fourth of the domain is simulated, and the section dimensions of the mold exit are 1600 mm × 263.5 mm. According to practical conditions, the narrow face taper of the TFM is 1.1 pct for microalloyed steel continuous casting. Consistent with the TFM, the NCM also has a taper of 1.1 pct to compensate for the corner shrinkage. Meanwhile, the bottom width of the NCM is identical to that of the TFM, and the top width of the NCM is 40 mm wider than that of the TFM because of the bulge at the narrow face top. By applying surface refinement, a Ni layer with a changing thickness is separated from the copper-based material. According to Meng and Thomas,^[1] the temperature gradient in molten steel (below 20 mm from the shell surface) is rather inconspicuous. Therefore, the liquid core is removed from the simulated

domain to reduce the computational cost. The thickness of the remaining section, which represents the solidifying shell and mushy zone, is 30 mm in the present work.

The thermomechanical model based on finite element technology describes the force–displacement relation with Eq. [1].

$$\mathbf{K}\mathbf{u}_s = \mathbf{F}, \quad [1]$$

where \mathbf{u}_s denotes the nodal displacement of the slab, \mathbf{K} denotes the stiffness matrix, and \mathbf{F} denotes the force vector.

The strain–displacement and stress–strain relations in terms of element nodal displacement are shown in Eqs. [2] and [3].

$$\boldsymbol{\varepsilon}_{el} = \boldsymbol{\beta}\mathbf{u}_{el}, \quad [2]$$

$$\boldsymbol{\sigma}_{el} = \mathbf{L}\boldsymbol{\varepsilon}_{el}, \quad [3]$$

where $\boldsymbol{\varepsilon}_{el}$ and $\boldsymbol{\sigma}_{el}$ denote the strains and stresses in the elements, respectively, and $\boldsymbol{\beta}$ and \mathbf{L} denote the strain–displacement and stress–strain relations, respectively. \mathbf{u}_{el} denotes the displacement vector associated with the element nodes.

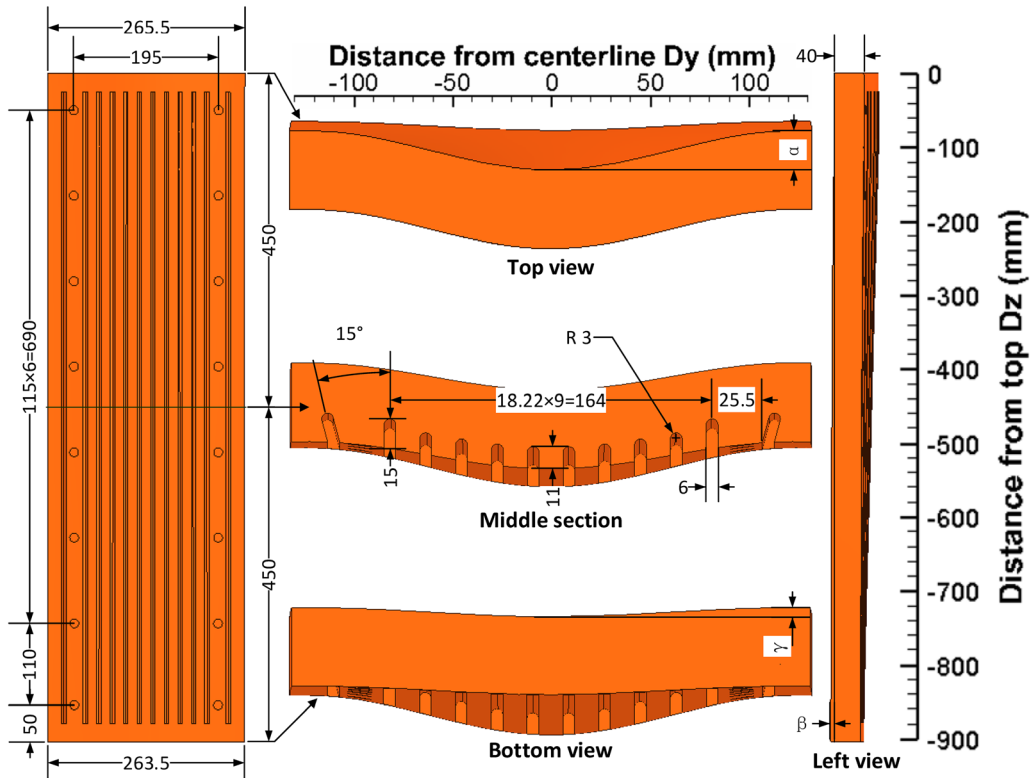


Fig. 3—Narrow face copper plate of the NCM.

The strand heat transfer is governed by Eq. [4]. The mold heat transfer is governed by Eq. [5].

$$\rho_s(T_s) \frac{\partial H(T_s)}{\partial t} = \nabla \cdot (k_s(T_s) \nabla T_s), \quad [4]$$

$$\rho_m c_m \frac{\partial T_m}{\partial t} = \nabla \cdot (k_m \nabla T_m), \quad [5]$$

where T_s and T_m are the temperatures of steel and copper plates, t is the current time, and $H(T_s)$, $\rho_s(T_s)$ and $k_s(T_s)$ denote the temperature-dependent enthalpy, density and conductivity of the steel, respectively, which are obtained according to the microsegregation model.^[25] k_m , ρ_m and c_m denote the conductivity, density and specific heat of the mold copper plates, whose values are assigned separately according to whether a Ni layer or copper-based material is considered. All of the thermal properties of the mold copper plates are listed in the existing literature.^[23]

Since the distortion of mold copper plates caused by thermal expansion is mainly concentrated at the meniscus and the deviation of taper compensation caused by this distortion is rather small,^[26] the mold copper plates are meshed as rigid bodies, and the strand deformable body. The temperature of the steel at the meniscus is initialized by the pouring temperature. The ferrostatic pressures loaded on the solidification front are calculated with Eq. [6].

$$P = \rho_s g h, \quad [6]$$

Table I. Geometric Parameters of the NCM

D_z (mm)	β (mm)	D_y (mm)	α (mm)	γ (mm)
-100	0.00	0	0	0.00
0	0.00	10	0.44	0.10
100	1.28	20	1.44	0.33
200	2.16	30	2.92	0.68
300	2.78	40	4.79	1.11
400	3.24	50	6.95	1.61
500	3.62	60	9.28	2.15
600	3.96	70	11.66	2.71
700	4.30	80	13.94	3.23
800	4.64	90	16	3.71
		100	17.71	4.11
		110	18.95	4.40
		120	19.61	4.55
		132.75	20	4.64

where g denotes the gravity acceleration, h denotes the metallic bath depth, and ρ_s denotes the molten steel density. Different from the common boundary conditions, the ferrostatic pressure should be loaded on the inner mesh. The detailed methods of tracking the solidification front and applying this boundary condition have been described in a study by Liu *et al.*^[27]

The nodal displacements of the slab symmetric planes can be expressed with Eq. [7]. In addition, those of the mold exit are expressed with Eq. [8].

$$\mathbf{u}_s \cdot \mathbf{n} = 0, \quad [7]$$

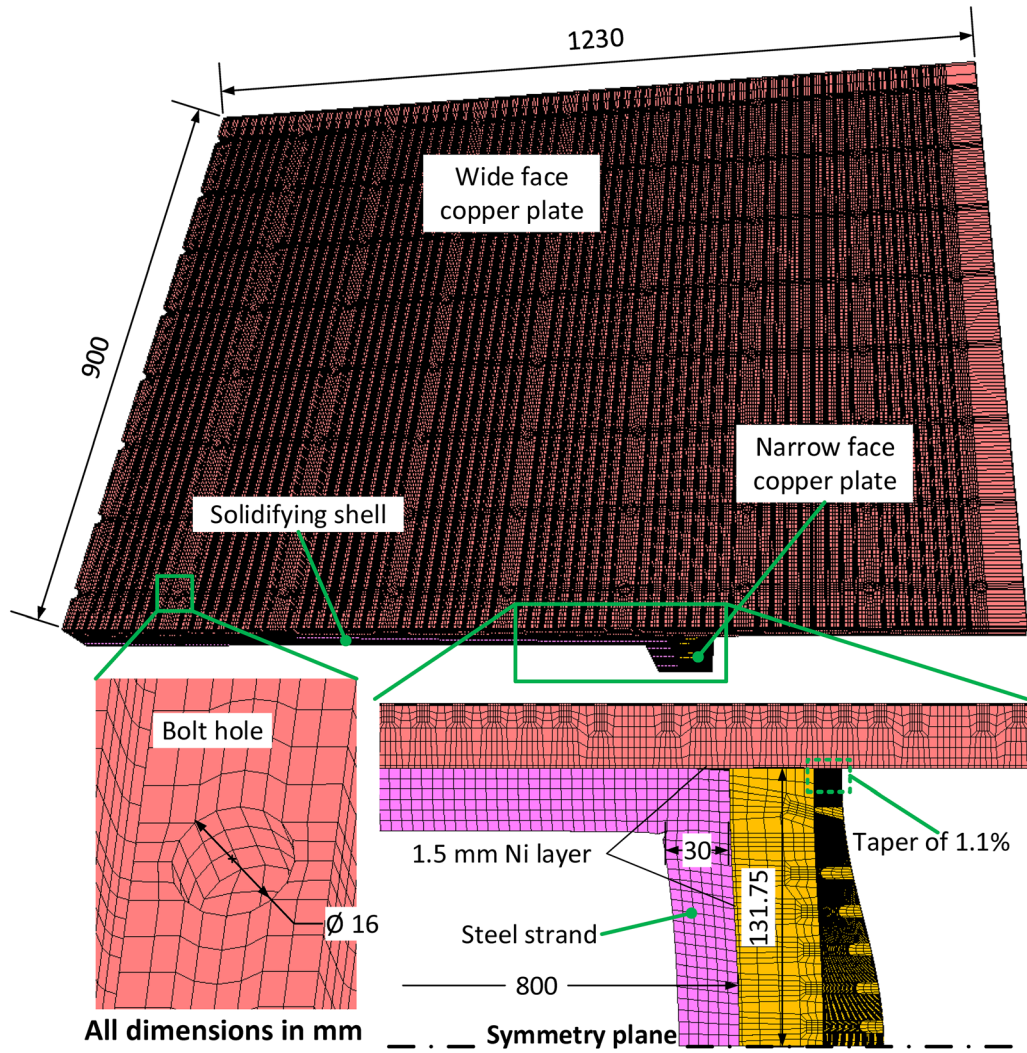


Fig. 4—Mesh details of the thermomechanical coupled model.

$$w = V_c \Delta t, \quad [8]$$

where \mathbf{n} denotes the normal vector, w denotes the displacement along the casting direction, and V_c is the casting speed.

Considering that many factors influence the heat transfer between the solidifying shell and mold copper plates, such as the properties and distributions of the mold slag layers, air gap expansion, and contact condition, an interface heat transfer model developed by Niu *et al.*^[23] is used in the present work to calculate the interfacial heat flux between the strand and mold copper plates. According to the model, there are three media at the shell–mold interface: liquid slag, solid slag and air. When the shell surface temperature is higher than the solidification temperature of the slag in the mold, the interface gap is filled with the liquid slag and solid slag; otherwise, it is filled with the solid slag and air. Based on the conservation of energy, the interfacial heat flux and distributions of the different media could be obtained by coupling with the thermomechanical

model. The thermal behavior in the water channels is calculated by the water flow and heat transfer model. Details of this model have been described previously by Niu *et al.*^[28]

The temperature-dependent elastic modulus and Poisson's ratio are obtained with Eqs. [9] and [10].^[29,30]

$$E = 968 - 2.33T_s + 1.9 \times 10^{-3}T_s^2 - 5.18 \times 10^{-7}T_s^3, \quad [9]$$

$$\nu = 0.278 + 8.23 \times 10^{-5}T_s. \quad [10]$$

According to the evolution of steel density during solidification, the thermal linear expansion coefficient (TLE) can be expressed by Eq. [11].

$$\text{TLE} = \sqrt[3]{\frac{\rho_{\text{ref}}}{\rho(T_s)}} - 1, \quad [11]$$

where ρ_{ref} and $\rho(T_s)$ are the steel densities at room temperature and T_s (in K).

2. 3D transient flow heat transfer and solidification model

Since the flow of molten steel has significant influences on the shell growth and temperature distribution, a 3D transient flow, heat transfer and solidification model is developed based on the TFM and NCM cavity structure. Figure 5 shows the mesh details and SEN geometry of the model. The mesh refinement technique is applied at the strand surface where solidification causes a considerable velocity sink. To avoid backflow, the length of the simulated domain is set to 3000 mm.

In this model, molten steel is assumed to be an incompressible Newtonian fluid. The flow and heat transfer of molten steel are governed by Eqs. [12], [13] and [16].^[31]

Continuity equation:

$$\frac{\partial \rho_s}{\partial t} + \nabla \cdot (\rho_s \mathbf{v}) = 0, \quad [12]$$

where \mathbf{v} is the velocity vector of molten steel.

Momentum equation:

$$\frac{\partial}{\partial t} (\rho_s \mathbf{v}) + \nabla \cdot (\rho_s \mathbf{v} \mathbf{v}) = -\nabla p + \nabla \cdot [\mu_{\text{eff}} (\nabla \mathbf{v} + \nabla \mathbf{v}^T)] + \rho_s \mathbf{g}_i + S_{\text{mon}}, \quad [13]$$

where p is the pressure, S_{mon} describes the momentum sink due to solidification, and μ_{eff} is the effective viscosity. S_{mon} and μ_{eff} can be obtained with Eqs. [14] and [15].

$$S_{\text{mon}} = \frac{(1 - f_l)^2 \times 10^8}{(f_l^3 + 0.001)} (\mathbf{v} - \mathbf{v}_p), \quad [14]$$

$$\mu_{\text{eff}} = \mu_l + \mu_t, \quad [15]$$

where \mathbf{v}_p is the casting velocity vector, f_l is the liquid fraction, μ_l is the apparent viscosity obtained from the solid fraction, and μ_t is the turbulent viscosity calculated by the low-Reynolds-number $k-\varepsilon$ model.

Energy equation:

$$\frac{\partial}{\partial t} (\rho_s H) + \nabla \cdot (\rho_s \mathbf{v} H) = \nabla \cdot (\lambda_{\text{eff}} \nabla T_s), \quad [16]$$

where

$$H = h_{\text{ref}} + \int_{T_{\text{ref}}}^{T_s} C_{ps} dT + f_l L. \quad [17]$$

H and h_{ref} denote the total and reference enthalpies. λ_{eff} denotes the effective thermal conductivity. C_{ps} and L denote the specific heat and latent heat of the steel.

The inlet of the submerged entry nozzle is set as a velocity inlet, and the bottom of the computational domain is set as a pressure outlet. The meniscus is set as an adiabatic plane, and the shear stresses are specified as 0. The moving speeds of the shell surfaces along the casting direction are defined according to the casting speed. The heat fluxes of the shell surfaces in the mold region are assigned based on the thermomechanical simulation. The properties of molten steel in this flow, heat transfer and solidification model are listed in Table II.

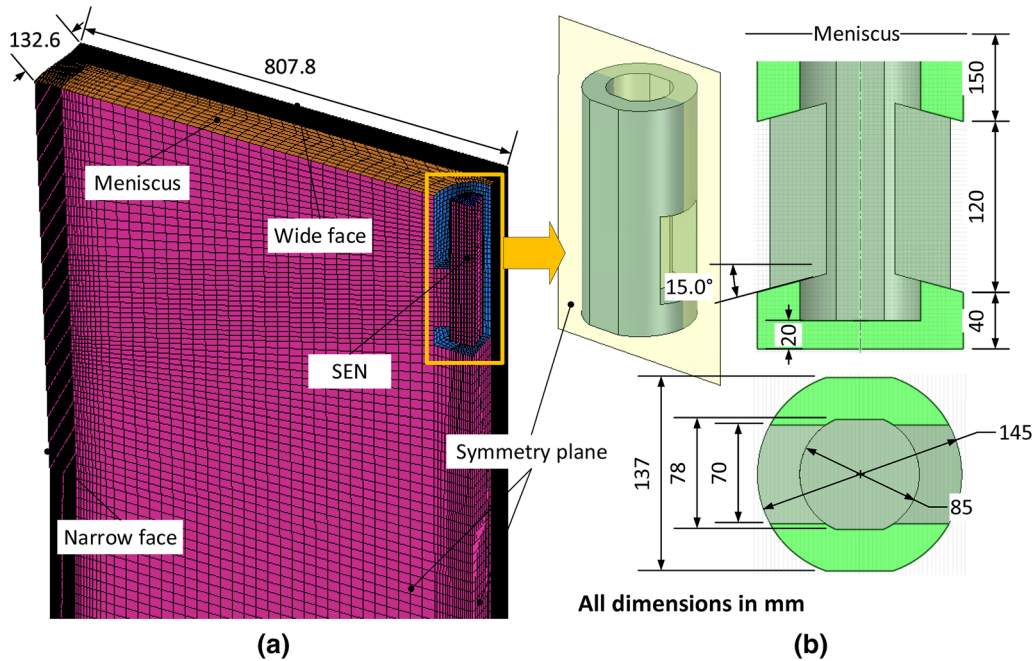


Fig. 5—Structure of the simulated domain: (a) mesh details and (b) SEN geometry.

C. Modeling Flow and Element Control

To investigate the effects of the mold design on the interfacial contact and heat transfer behaviors in the TFM and NCM, the nonlinear finite element software MSC Marc is applied to solve the thermomechanical model. By calling the subroutine, which could deactivate/activate the elements, steel is continuously generated at the meniscus. Similarly, the strand elements were deactivated when they moved out of the mold region. Furthermore, the subroutine, which is used to define the heat transfer between contact areas, was called to couple the thermomechanical model with the interface heat transfer model. The interface heat transfer model has been described in previous work.^[23] In the calculation, the temperatures of the shell surface and mold hot face and their contact distance are delivered from the thermomechanical model to the interface heat transfer model. After that, the interfacial heat fluxes and dynamic distributions of the mold slag layers and air gaps are calculated by the interface heat transfer model and returned to the thermomechanical model. After completion of the thermomechanical analysis, the interfacial heat fluxes between the mold and solidifying shell are exported and loaded into the flow heat transfer and solidification model as boundary conditions. Solving the model by the CFD software Fluent, the temperature and growth of the solidifying shell are thoroughly compared between the TFM and NCM.

III. RESULTS AND DISCUSSION

A. Model Validation

Since the thermomechanical model couples the analysis of dynamic mold slag distributions, the slag layers attached at the TFM hot faces are collected to validate the model. Figure 6 shows the comparison of wide face slag layers calculated and measured at the mold exit under the simulated operation conditions shown in Table III. The measured thickness of the solid slag layer reaches 1.5 mm at 5 mm off the corner, which is 0.2 mm thinner than the calculated thickness. In the area 10 mm off the corner, the measured thickness is close to the calculated thickness and reaches approximately 1.9 mm. Another piece of slag layer shows that the thickness decreases to 1 mm at 80 mm off the corner. Meanwhile, the calculated thickness of the solid slag layer has an

Table II. Thermophysical Properties of Steel

Thermophysical Properties	Value
Density (kg/m ³)	7200
Liquidus Temperature (K)	1789
Solidus Temperature (K)	1737
Thermal Conductivity (W/(m K))	34
Latent Heat (J/kg)	270,000
Viscosity (kg/(m s))	0.0062
Specific Heat (J/(kg K))	680

identical downtrend. Influenced by the surface tension, the measured corner thickness is greater than 2 mm, which is inconsistent with the calculated corner thickness. However, the consistency between the calculated and measured thicknesses of the solid slag layers in the off-corner and center areas demonstrates the validity of the thermomechanical model.

Considering that the slag layers could lubricate the interface between the mold and strand, the wear of the TFM copper plates is used to validate the predicted distributions of the mold slag layers, as shown in Figure 7. Since the liquid slag layer could lubricate the contact interface adequately, there is no significant wear at the upper part of the mold. The W-shaped stain left by the liquid slag layer coincides well with the calculated distribution of the liquid slag layer. At the lower part of the mold, the solid slag layer is evenly distributed at the narrow face center, which could efficiently protect the area from wear. Meanwhile, the shell corner, which is covered by a thicker solid slag layer, has a lower temperature and higher stiffness. Under mold oscillation, heavy wear forms at the narrow face corner. In summary, the stain and wear of the narrow face copper plate show good consistency with the calculated distributions of mold slag layers.

Signals recorded by the thermocouples in the mold copper plates are compared with the calculated temperatures of the mold, as shown in Figure 8. Comparing the signals of the different rows of thermocouples, the mold temperature decreases along the casting direction. The average temperatures of TC1, TC2, and TC3 are 395 K, 382 K, and 369 K, respectively, which are close to the temperatures calculated at the wide face centerline, as shown in Figure 8(a). For the narrow face, a similar consistency between the measured and calculated temperatures appears at the centerline.

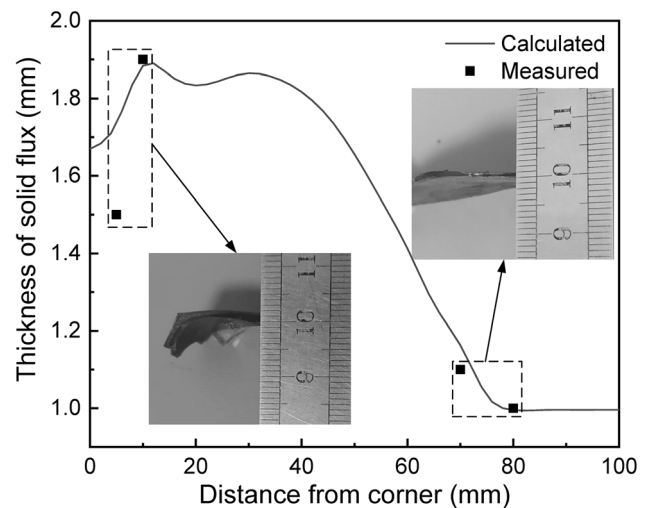


Fig. 6—Distribution of solid slag layer at the wide face.

B. Contact Behavior

The contact condition between the shell and mold copper plates has a significant influence on the interfacial heat transfer, which deteriorates the surface quality of the slab in the condition of a nonuniform distribution. Based on the thermomechanical coupled model, the interfacial contact behaviors in the TFM and NCM are compared and shown in Figure 9. To highlight the distortion of the solidifying shells, the contact gaps between the strands and molds are magnified up to 3 times. As shown in Figure 9(a), the slab corner in the TFM begins to shrink away from the mold walls at 100 mm below the meniscus and leaves very small interfacial gaps at both the wide and narrow faces. In the corner of the NCM, a similar gap appears at the wide face corner, while the narrow face copper plate is in close contact with the shell. With the shell moving down to 300 mm

Table III. Typical Casting Conditions

Items	Value
Effective Mold Height (mm)	800
Slab Section Dimensions (mm)	1600 × 263.5
Pouring Temperature (K)	1814
Narrow Face Taper (%)	1.10
Casting Speed (m/min)	1.05
Wide Face Water Flow (L/min)	4760
Narrow Face Water Flow (L/min)	530
Import Water Temperature (K)	305
Main Compositions of Steel (%)	Niu <i>et al.</i> ^[23]
Properties of the Mold Slag	Niu <i>et al.</i> ^[23]

below the meniscus, the ranges of the expansion areas in the TFM reach 79 mm at the wide face and 52 mm at the narrow face. By contrast, the corner gaps in the NCM have no significant expansion. With the shrinkage of the slab corner getting moderated at the lower middle part of the TFM, the gap at the narrow face begins to narrow under the compensation of the narrow face taper. Since the wide face can hardly obtain adequate compensation, the corner gap at the wide face of the TFM continues to expand at the lower part of the mold. For the NCM, neither the wide face nor narrow face significantly expands the corner gap. The range of the wide face expansion area is maintained below 15 mm.

C. Distributions of Interfacial Heat Transfer Media

Figure 10 shows the distributions of the liquid slag layers in different types of molds under the same operating conditions. Despite the different cavity structures, the longitudinal distributions of the liquid slag layers show similar trends along the casting direction in both the TFM and NCM. At the meniscus, the liquid slag layers become thicker as the initial solidifying shells move downward. The maximum thicknesses are observed at 47 mm below the meniscuses, and then the liquid slag layers begin to thin in the center, corner and off-corner areas. Since the expansion of corner gaps leads to the filling of liquid slag in those areas, the liquid slag layers in the off-corner areas remain thicker than those in the center areas. Compared with the TFM, the NCM reduces the maximum thickness at the narrow face from 0.24 to 0.21 mm. Moreover, Figures 10(a) and (b) show an obvious hysteretic solidification of the

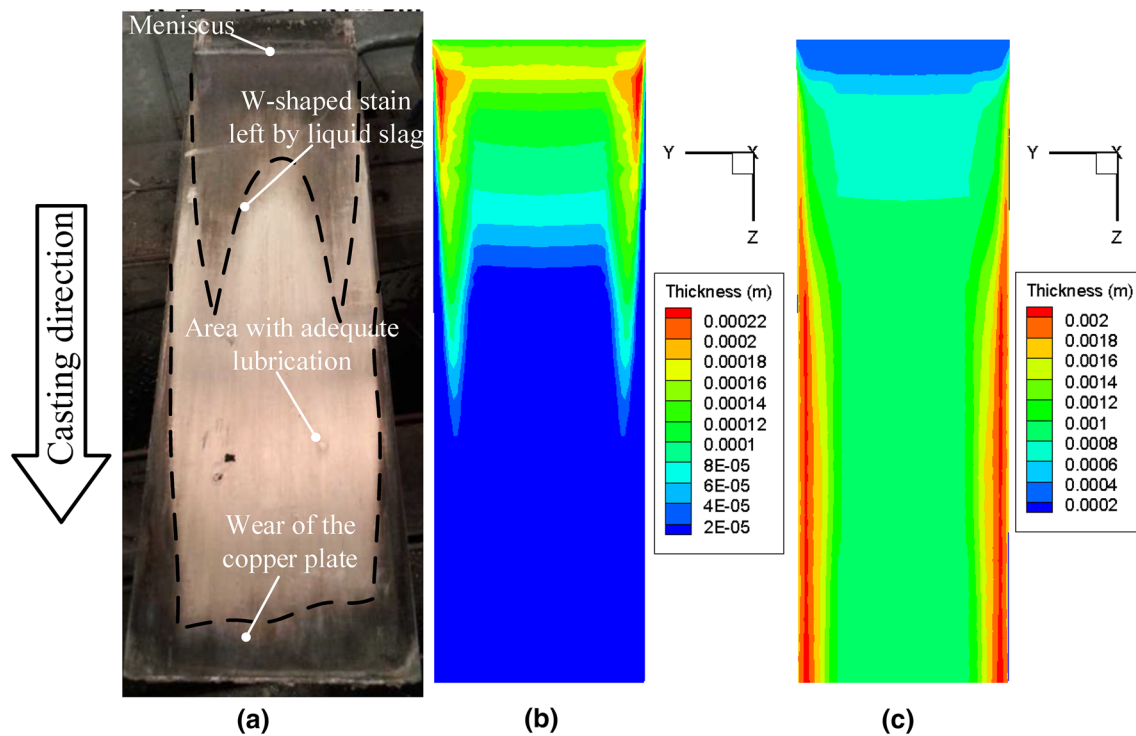


Fig. 7—Comparison between the (a) mold wear and thickness distributions of the (b) liquid slag and (c) solid slag.

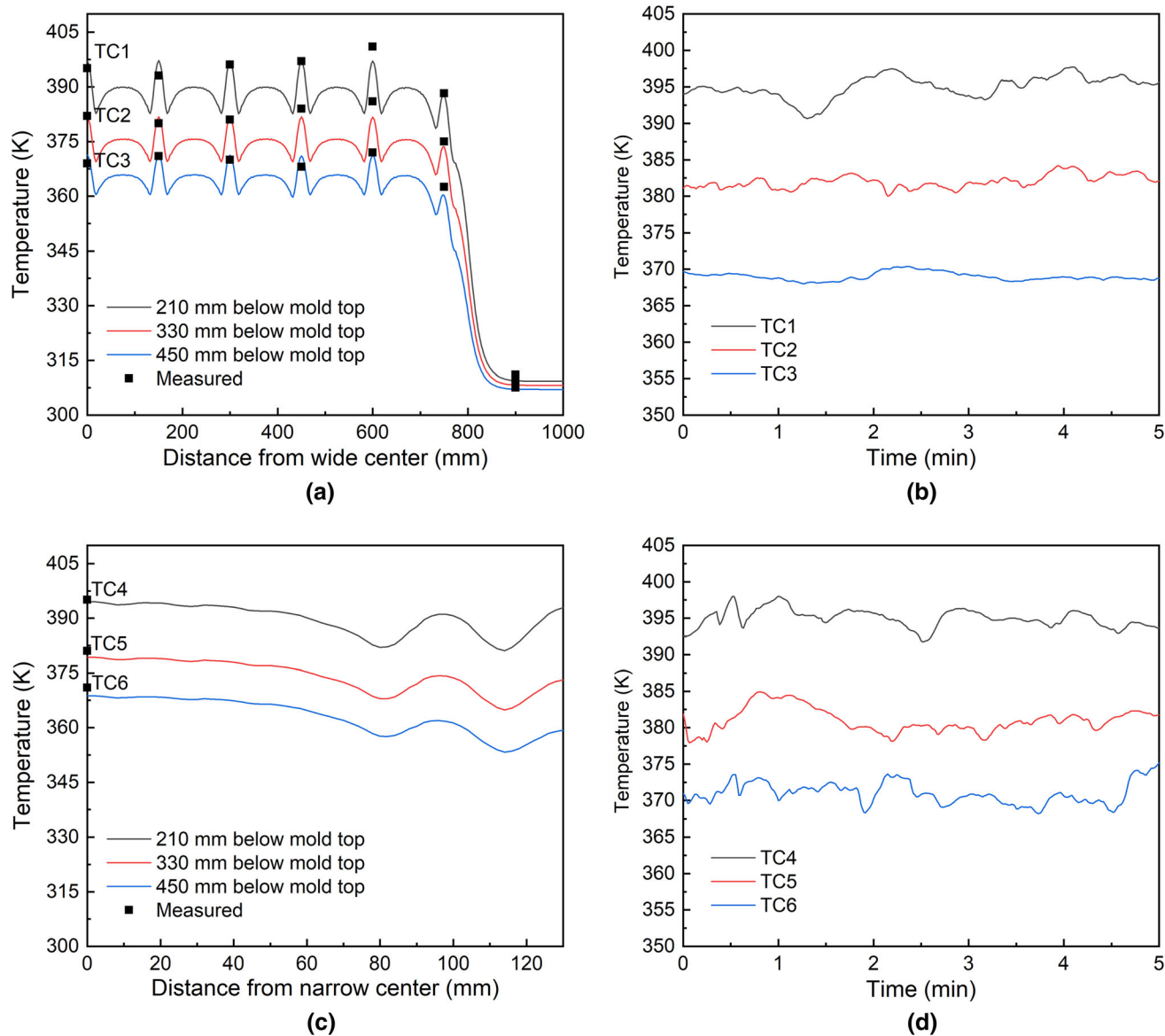


Fig. 8—Comparison between the calculated and measured mold temperatures: (a) wide face comparison, (b) wide face signal, (c) narrow face comparison, and (d) narrow face signal.

liquid slag in the off-corner areas, which would deteriorate the homogeneity of the heat transfer there. In the NCM, the endpoint of the wide face off-corner liquid slag is elevated from 612 mm below the meniscus to 310 mm, and that of the narrow face is elevated from 540 to 360 mm.

The distributions of interfacial solid mold slag layers in different types of molds are shown in Figure 11. Along the casting direction, the solid slag layers become thicker as the surface temperatures of the solidifying shells decrease. In the center areas of the wide and narrow faces, where the shells maintain close contact with the mold hot faces, the evolutions of the solid slag layers in the NCM have trends similar to those in the TFM. However, the corner and off-corner areas show significant differences between the NCM and TFM. In the TFM, a thick solid slag layer covers up to 82 mm of

the wide face corner, and that of the narrow face ranges up to approximately 52 mm. The corner liquid slag completely solidifies 83 mm below the meniscus, where the wide face solid slag layer reaches a thickness of 1.64 mm and the narrow face reaches a thickness of 1.68 mm. At the TFM off-corner areas approximately 295 mm below the wide face meniscus and 340 mm below the narrow face, the solid slag layers reach their maximum thicknesses of 1.88 and 2.06 mm, respectively. Compared with the TFM, the distributions of solid slag layers in the NCM are more homogeneous, especially for the narrow face. The maximum thicknesses of the solid slag layers at the wide and narrow faces of the NCM decrease to approximately 1.61 and 1.28 mm, respectively. The coverage of the thick slag layer in the wide face off-corner area decreases to 24 mm, and that at the narrow face becomes inconspicuous.

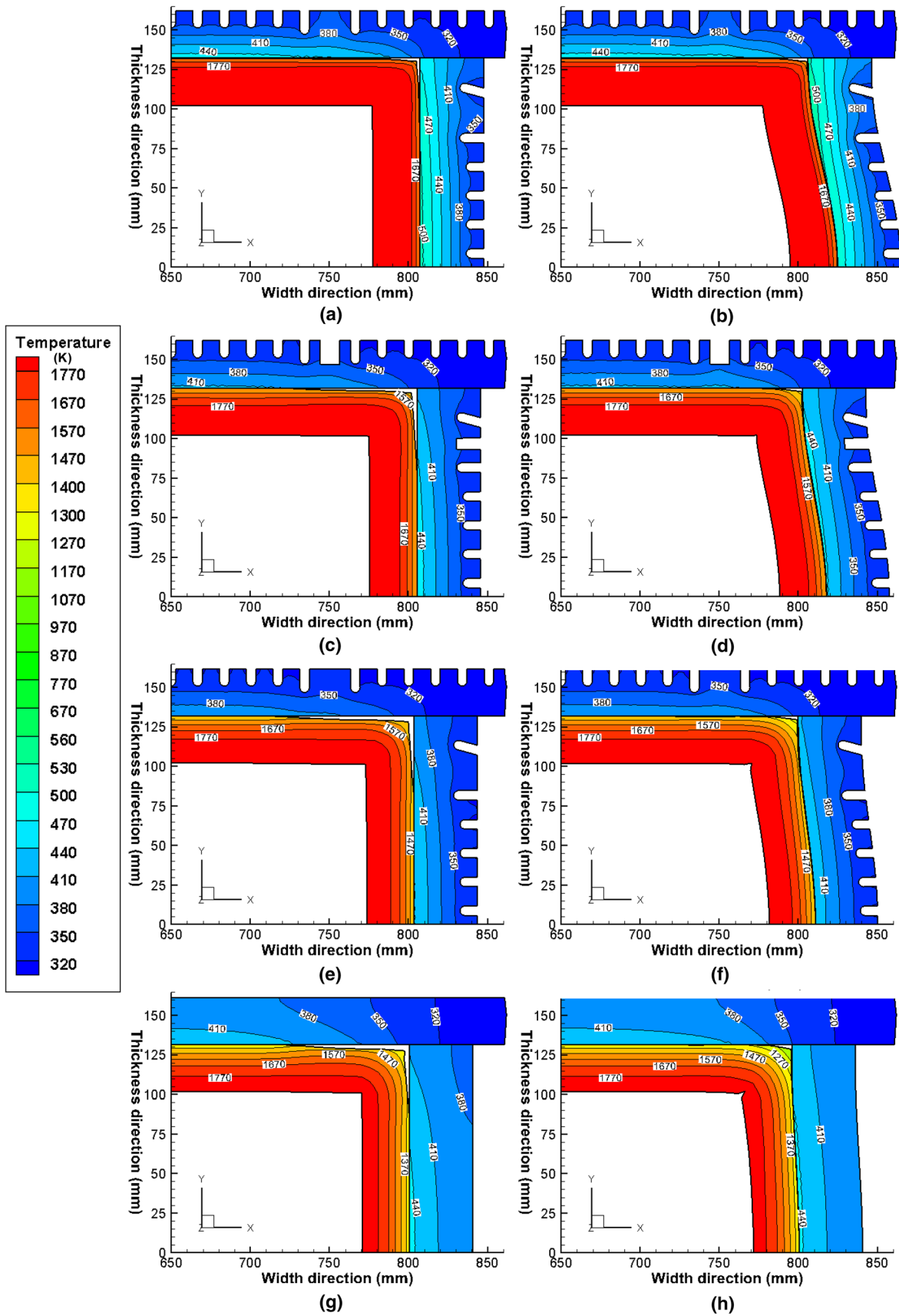


Fig. 9—Shell distortion in the TFM and NCM at the positions of (a, b) 100 mm, (c, d) 300 mm, (e, f) 500 mm, and (g, h) 800 mm below the meniscus.

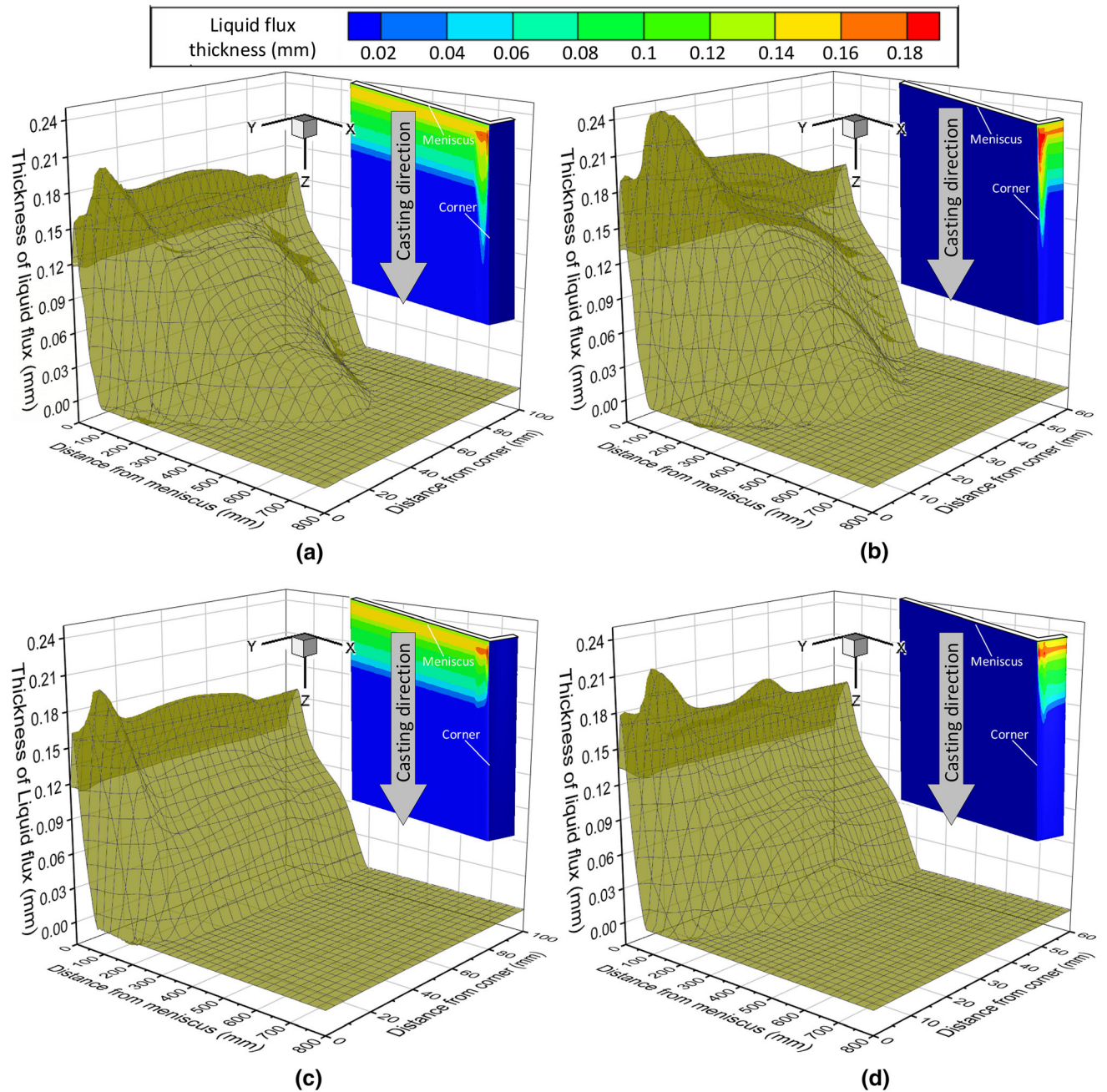


Fig. 10—Thickness of the interfacial liquid slag layer: (a) wide face of the TFM, (b) narrow face of the TFM, (c) wide face of the NCM, and (d) narrow face of the NCM.

The air gap has a significant influence on the thermal profile of the solidifying shell because of its excellent adiabaticity. This usually leads to a considerable nonuniform distribution of shell temperature, which should be avoided during continuous casting. The distributions of the air gaps in the different types of molds are shown in Figure 12. The air gaps are concentrated in the corner and off-corner areas. At the wide face of the TFM, the air gap initially forms 83 mm below the meniscus. As the shell moves downward, the interfacial air gap begins to expand. At 325 mm below the meniscus, the liquid slag layer 84 mm off the shell corner completely solidifies. Afterward, the continuous

corner shrinkage causes the air gap to expand to the off-corner area. At the mold exit, the corner air gap reaches a thickness of 0.63 mm, and that of the off-corner reaches a thickness of 0.13 mm. The TFM narrow face shows a quite different distribution of air gap, as illustrated in Figure 12(b). The maximum thickness (approximately 0.5 mm) appears 400 mm below the meniscus. With the shell shrinkage moderated at the lower part of the mold, the corner air gap is pinched by the taper compensation of the narrow face. Finally, it decreases to 0.12 mm at the mold exit. In the NCM, the shrinkage of the shell corner is controlled by reasonable compensation at both the wide and narrow

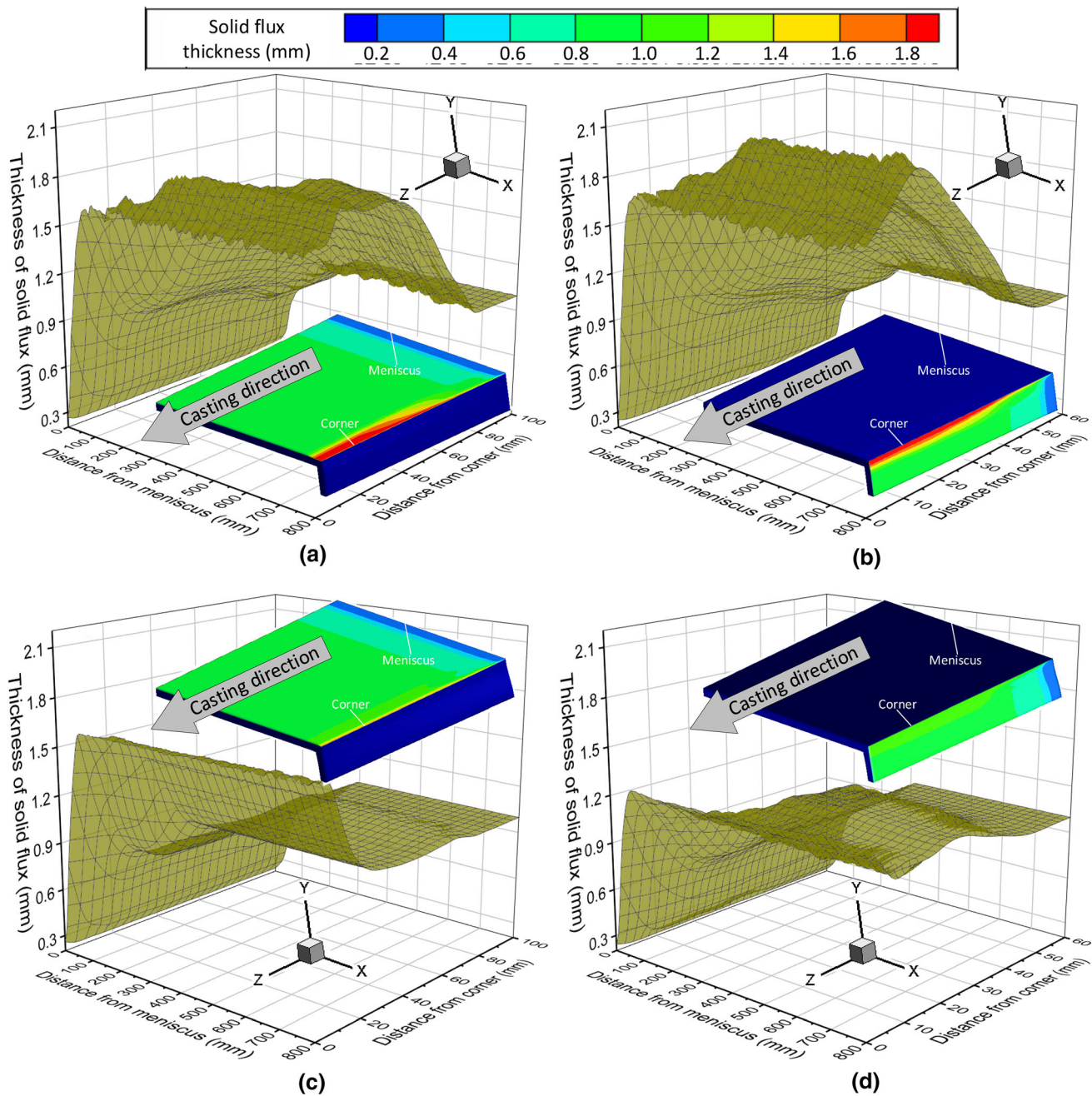


Fig. 11—Thickness of the interfacial solid slag layer: (a) wide face of the TFM, (b) narrow face of the TFM, (c) wide face of the NCM, and (d) narrow face of the NCM.

faces. As a result, the air gaps in the corner and off-corner areas are significantly reduced. At the wide face of the NCM, the air gap concentrates within 15 mm off the corner, and the maximum thickness is reduced to 0.31 mm at the mold exit. Furthermore, the air gap in the off-corner area is eliminated completely. Figure 12(d) shows that no significant air gap appears at the narrow face. The thickest air gap (approximately 0.16 mm) appears 345 mm below the meniscus and 8 mm off the corner. Near the mold exit, the air gap at the narrow face completely disappears.

D. Shell Growth and Temperature Distribution

The distributions of the mold slag layers have definite influences on the interfacial heat flux between the mold and strand, as shown in Figure 13. In both the TFM and NCM, the heat fluxes of the different spots increase rapidly above the meniscus and reach their maximums at 7.5 mm below the meniscus. After that, the heat fluxes decrease down the mold and fluctuate beneath the bolt holes. The decreases in heat fluxes are moderate 100 mm below the meniscus. Limited by the structure of the water channels, the cooling water cannot reach the mold bottom. Therefore, the heat fluxes show significant

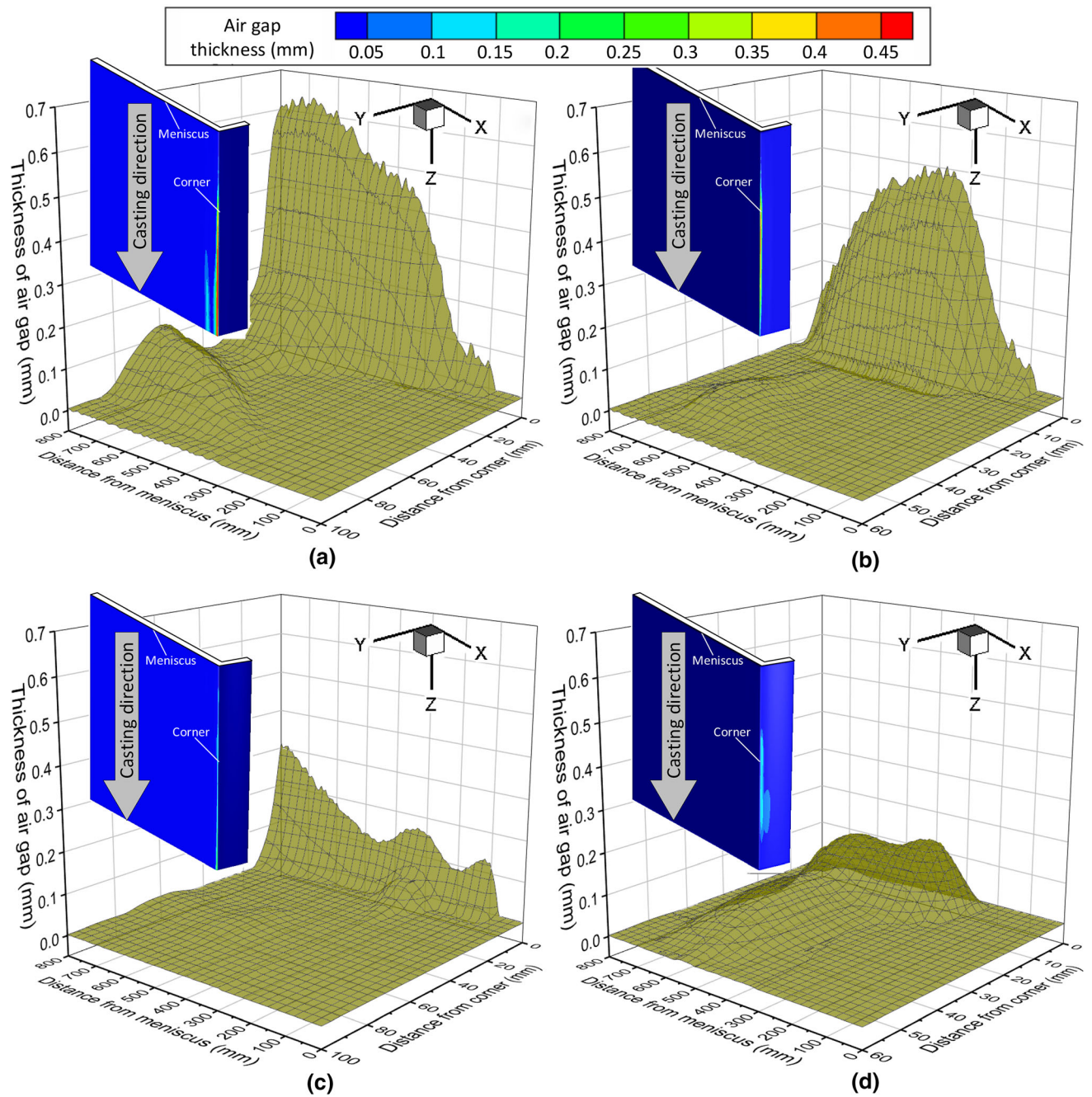


Fig. 12—Thickness of the interfacial air gap: (a) wide face of the TFM, (b) narrow face of the TFM, (c) wide face of the NCM, and (d) narrow face of the NCM.

decreases near the mold exit. Considering that the coverage of the wide face contact gap in the TFM is wider than that of the narrow face, the wide face heat fluxes at 40 mm off the corners are compared between the TFM and NCM, as well as the narrow faces at 30 mm off the corners. To reduce the impact of channel depth on the transverse comparison, the wide face interfacial heat fluxes are compared at 40 and 640 mm off the corner, where the channels have similar depths and layouts. Apparently, the NCM has a more homogeneous distribution of interfacial heat fluxes in the off-corner areas. From 100 mm below the meniscus to

the mold exit, the average heat flux differences between the off-corner (40 mm off the corner at the wide face and 30 mm off the corner at the narrow face) and center areas reach 0.24 and 0.28 MW/m² at the wide and narrow faces of the TFM, respectively. For the NCM, the average differences reach 0.01 and 0.16 MW/m² at the wide and narrow faces.

Loading the interfacial heat fluxes on the flow heat transfer and solidification model, the convective and conductive heat transfer in the strand could be simulated. Figure 14 shows the temperatures of the shell surfaces in the TFM and NCM. The shells in different

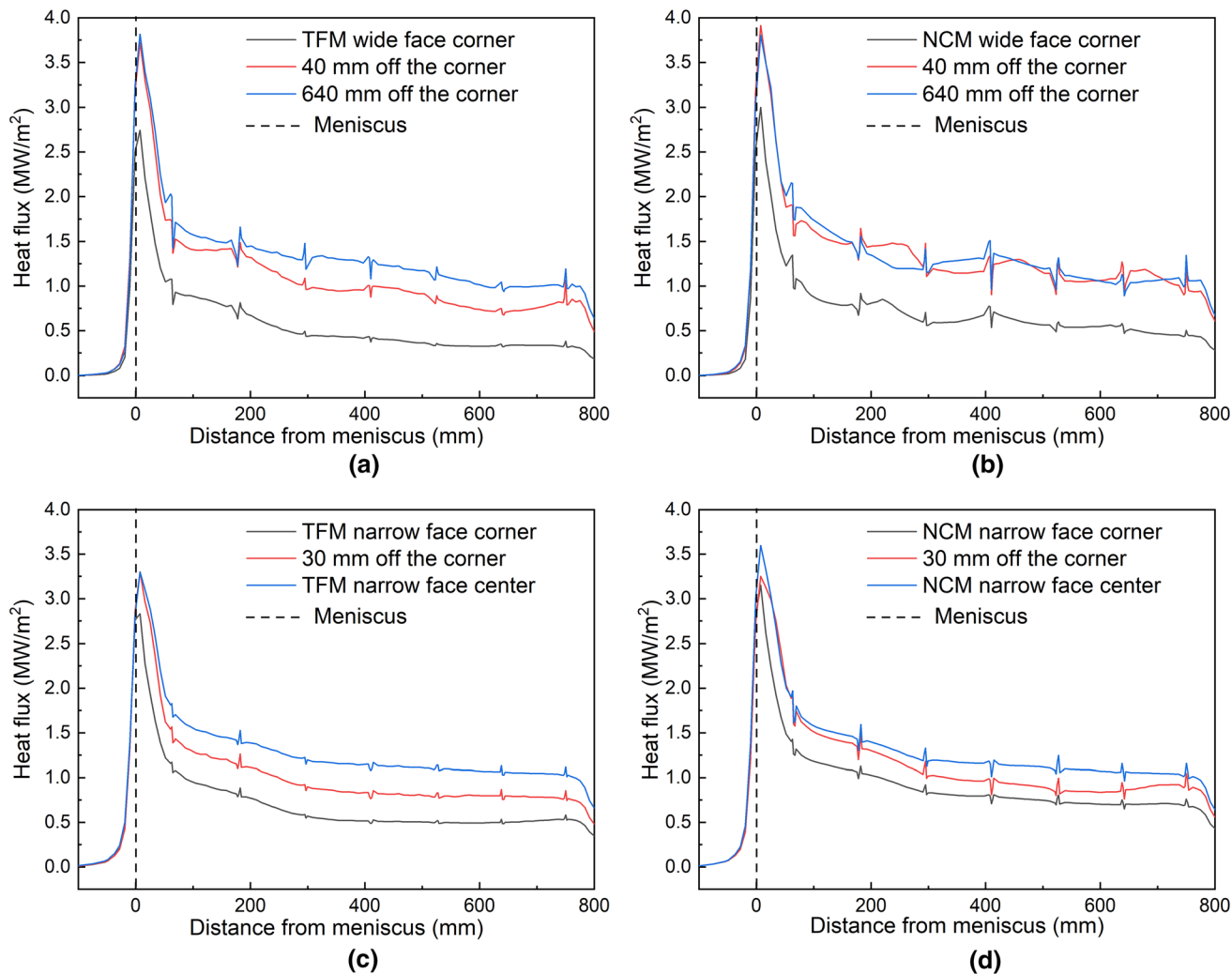


Fig. 13—Interfacial heat flux between the mold and strand: (a) wide face of the TFM, (b) wide face of the NCM, (c) narrow face of the TFM, and (d) narrow face of the NCM.

molds have similar temperature distributions at the mid-face areas. Near the meniscus, the shell surface temperatures are distributed homogeneously. Along the casting direction, the temperatures of the shell surfaces decrease at different rates, which leads to nonuniform distributions. At 250 mm below the meniscus, the areas beneath the deep channels are significantly colder than those beneath the shallow channels, by approximately 28 K. At the mold exit, the temperatures of the wide and narrow midfaces reach 1308 K and 1323 K, respectively. What should be noted is that the TFM has higher temperatures in the off-corner areas, which is mainly caused by the thick slag layers and air gap expansions. Meanwhile, the NCM homogenizes the temperatures of off-corner areas and enhances the cooling of the shell corner. At the mold exit, the corner temperatures of the TFM and NCM reach 1088 K and 931 K, respectively.

Figure 15 shows the cooling rates of the shell corners in the TFM and NCM. Within 200 mm of the meniscus, the cooling rates of the shell corners in the different types of molds show a similar decrease. With the expansion of the corner air gap, the cooling rate of the

TFM decreases to 3.3 K/s at 300 mm below meniscus. After that, the cooling rate remains at a low level, and the average cooling rate from 300 mm below the meniscus to the mold exit is 4.73 K/s. Compared with the TFM, the NCM can more efficiently improve the corner cooling rate in the primary cooling stage. The minimum cooling rate of the shell corner is 5.98 K/s, and the average cooling rate of the lower part of the mold is increased to 8.18 K/s.

The effect of mold design on the homogeneity of shell growth is shown in Figure 16. The model is validated by predicting a shell thickness close to that of the measured breakout shell. At the wide faces, the TFM has a large difference in shell thicknesses between the wide face center and off-corner. This difference is inconspicuous at the upper part of the mold. As the shell moves into the lower part, the thick slag layers and air gaps in the corner and off-corner areas impede the heat transfer between the mold and strand. Accordingly, the growth of the shell in the off-corner area begins to slow. At the mold exit, the thickness difference between the wide face center and off-corner reaches 2.1 mm. For the narrow

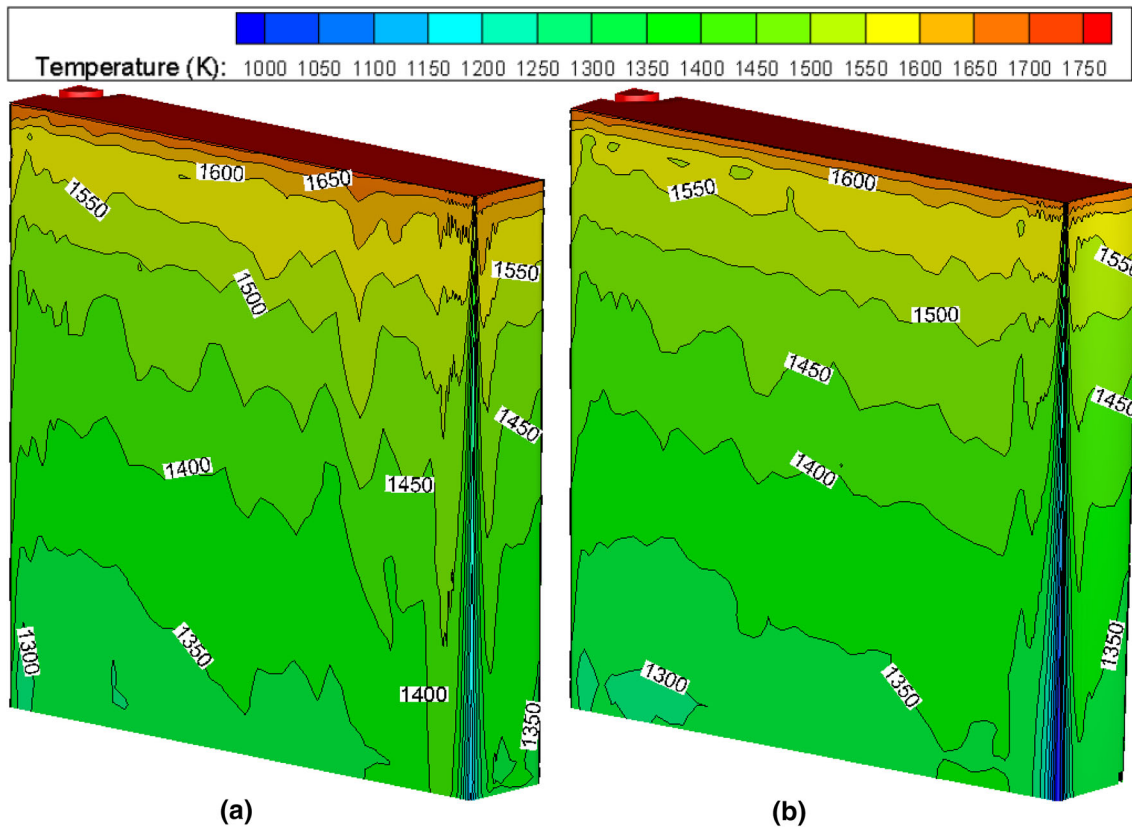


Fig. 14—Temperatures of the shell surfaces in the (a) TFM and (b) NCM.

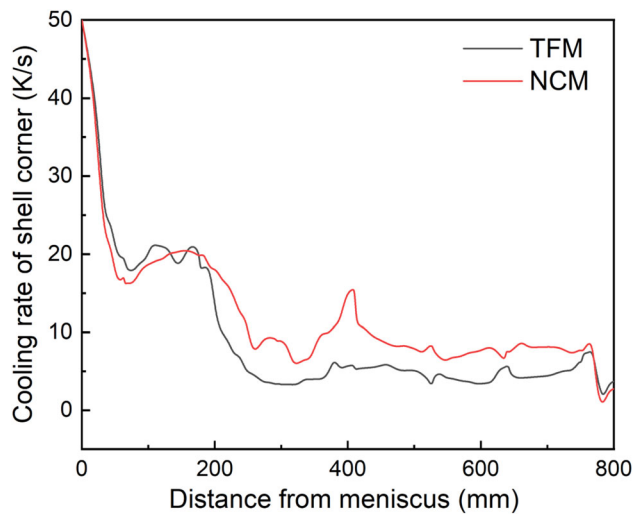


Fig. 15—Cooling rates of the shell corners in the TFM and NCM.

face, the shell thickness difference increases first, reaches a maximum at 450 mm below the meniscus and then begins to decrease. Impinged by the high-temperature molten metal stream, shell growth of the narrow face center slows at the lower part of the mold, while the multidimensional cooling of the shell corner accelerates the off-corner shell growth. Therefore, the narrow face off the corner becomes thicker than the narrow face center at the mold exit. Compared with the TFM, the

shell growth in the NCM is more homogeneous. The differences between the wide face center and off-corner areas are inconspicuous at the mold exit. For the narrow face, the off-corner shell is approximately 1 mm thicker than the center at the mold exit.

IV. CONCLUSIONS

A convex structure mold was designed to intensify cooling on the shell corner and help implement double phase-transformation technology in the high-temperature cooling zone of casters during microalloyed steel continuous casting. To fully utilize the advantages of the NCM, a thermomechanical model coupled with a flow heat transfer and solidification model was developed in the present work; with this model, the effects of mold design on the thermal, deformation, and solidification behaviors of slab strands were evaluated and compared between the TFM and NCM. Based on the simulation, the following conclusions could be drawn:

1. The TFM exhibits large interfacial gaps between the mold and strand at the corner and off-corner areas, which contribute to the nonuniform distributions of the mold slag layers and insufficient cooling of the shell corner. In the NCM, the shell corner shrinkage along the width direction obtains a suitable nonlinear compensation, while the expansion of the narrow

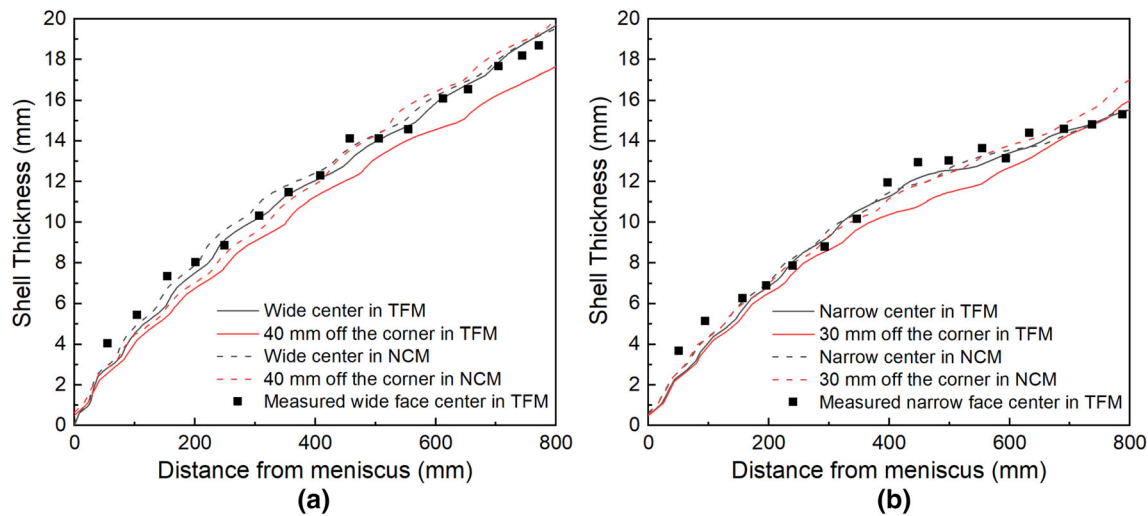


Fig. 16—Shell growths at the (a) wide and (b) narrow faces.

face reduces the interfacial gap at the wide face corner.

- Thick slag layers appear at the corner and off-corner areas in the TFM. The maximum thicknesses reach 1.88 mm at the wide face and 2.06 mm at the narrow face. Meanwhile, those in the center areas are only 1 mm thick. The NCM could homogenize the distributions of mold slag layers and limit the maximum thicknesses to 1.61 mm at the wide face and 1.28 mm at the narrow face.
- The air gap at the wide face corner of the TFM continuously expands after it initially forms 83 mm below the meniscus. That at the narrow face first increases at the upper part of the mold and then decreases at the lower part. The maximum thicknesses of the air gap at the wide and narrow faces reach 0.63 and 0.5 mm, which could be reduced to 0.31 and 0.16 mm in the NCM.
- The thick slag layers and air gap in the corner and off-corner areas lead to nonuniform distributions of shell corner temperature and shell growth in the TFM. Hot spots appear at the wide and narrow face off-corner areas. At the mold exit, the shell thickness of the wide face off-corner area is 2.1 mm thinner than that of the wide face center. The NCM can eliminate hot spots by enhancing cooling in corner and off-corner areas. As a result, the temperature of the shell corner decreases from 1088 K to 931 K in the NCM.

ACKNOWLEDGMENTS

This work was financially supported by the National Natural Science Foundation of China (51774075, 51404061) and Fundamental Research Funds for the Central Universities of China (N182504013).

REFERENCES

- Y. Meng and B.G. Thomas: *Metall. Mater. Trans. B*, 2003, vol. 34B, pp. 685–705.
- C. Li and B.G. Thomas: *Metall. Mater. Trans. B*, 2004, vol. 35B, pp. 1151–72.
- J.K. Park, C. Li, B.G. Thomas, and I.V. Samarasekera: *60th Electr. Furn. Conf.*, San Antonio, TX, 2002, AIST, Warrendale, PA, 2002, vol. 60, pp. 669–86.
- D.J. Jing and K.K. Cai: *Acta Metall. Sin.*, 2000, vol. 36, pp. 403–06.
- C. Li, and B.G. Thomas: *ISSTech Steelmak. Conf.*, Indianapolis, IN, USA, 2003, ISS-AIME, Warrendale, PA, 2003, pp. 685–700.
- B.G. Thomas and C. Ojeda: *ISSTech Steelmak. Conf.*, Indianapolis, IN, USA, 2003, ISS-AIME, Warrendale, PA, 2003, pp. 295–308.
- Y.M. Won, T.J. Yeo, K.H. Oh, J.K. Park, J. Choi, and C.H. Yim: *ISIJ Int.*, 1998, vol. 38, pp. 53–62.
- R.B. Mahapatra, J.K. Brimacombe, and I.V. Samarasekera: *Metall. Mater. Trans. B*, 1991, vol. 22B, pp. 875–88.
- J.K. Brimacombe, F. Weinberg, and E.B. Hawbolt: *Metall. Trans. B*, 1979, vol. 10B, pp. 279–92.
- N. Yamasaki, S. Shima, K. Tsunenari, S. Hayashi, M. Doki, Y. Kato, D. Miki, and T. Nakanishi: *Nippon Steel Sumitomo Met. Tech. Rep.*, 2016, vol. 112, pp. 64–70.
- S.N. Berdnikov, A.E. Pozin, A.A. Podosyan, A.S. Berdnikov, V.A. Mokhov, and K.N. Vdovin: *Steel Transl.*, 2012, vol. 42, pp. 180–82.
- Z. Cai and M. Zhu: *ISIJ Int.*, 2013, vol. 53, pp. 1818–27.
- J.K. Brimacombe and K. Sorimachi: *Metall. Trans. B*, 1977, vol. 8B, pp. 489–505.
- P. Hu, H. Zhang, M. Wang, M. Zhu, X. Zhang, Y. Zhang, and Z. Zhang: *Metall. Res. Technol.*, 2015, vol. 112, pp. 104–13.
- S. Yu, M Long, D. Chen, H. Fan, H. Yu, H. Duan, X. Xie, and T. Liu: *J. Mater. Process. Technol.*, 2019, vol. 270, pp. 157–67.
- P. Lyu, W. Wang, X. Long, K. Zhang, E. Gao, and R. Qin: *Metall. Mater. Trans. B*, 2017, vol. 49B, pp. 78–88.
- S.V. Filatov, A.I. Dagman, V.N. Karavaev, V.P. Glebov, G.N. Kononykhin, A.B. Kotel'nikov, and A.A. Vopneruk: *Metallurgist*, 2018, vol. 62, pp. 58–61.
- F.J. Ma, G.H. Wen, P. Tang, X. Yu, J.Y. Li, G.D. Xu, and F. Mei: *Ironmak. Steelmak.*, 2010, vol. 37, pp. 73–79.
- T. Kato, Y. Ito, M. Kawamoto, A. Yamanaka, and T.J.I. Watanabe: *ISIJ Int.*, 2003, vol. 43, pp. 1742–50.
- C. Du, J. Zhang, J. Wen, Y. Li, and P. Lan: *Ironmak. Steelmak.*, 2016, vol. 43, pp. 331–39.
- J. Liu, G. Wen, and P. Tang: *Metall. Mater. Trans. B*, 2017, vol. 48B, pp. 3074–82.
- F.J. Ma, G.H. Wen, P. Tang, X. Yu, J.Y. Li, G.D. Xu, and F. Mei: *Ironmak. Steelmak.*, 2010, vol. 37, pp. 211–18.

23. Z. Niu, Z. Cai, and M. Zhu: *ISIJ Int.*, 2019, vol. 59, pp. 283–92.
24. MSC Marc: *Theory and User Information*, MSC Software Corporation, Newport Beach, 2016.
25. Z. Cai and M. Zhu: *Acta Metall. Sin.*, 2011, vol. 47, pp. 671–77.
26. X. Liu and M. Zhu: *ISIJ Int.*, 2006, vol. 46, pp. 1652–59.
27. K. Liu, Y.H. Chang, Z.G. Han, and J.Q. Zhang: *J. Iron Steel Res. Int.*, 2013, vol. 20, pp. 38–47.
28. Z. Niu, Z. Cai, and M. Zhu: *Ironmak. Steelmak.*, 2019, vol. 47, pp. 1135–47.
29. H. Mizukami, K. Murakami, and Y. Miyashita: *Tetsu-to-Hagane*, 1977, vol. 63, p. 652.
30. M. Uehara, I.V. Samarasekera, and J.K. Brimacombe: *Ironmak. Steelmak.*, 1986, vol. 13, pp. 138–53.
31. ANSYS Inc.: *ANSYS FLUENT 16.2 Theory Guide*, ANSYS, Inc., Canonsburg, 2015.

Publisher's Note Springer Nature remains neutral with regard to jurisdictional claims in published maps and institutional affiliations.